Phys. Med. Biol. 40 (1995) 1651–1664. Printed in the UK

Analysis and correction of geometric distortions in 1.5 T magnetic resonance images for use in radiotherapy treatment planning

M A Moerland†, R Beersma†, R Bhagwandien†, H K Wijrdeman† and C J G Bakker‡

† Department of Radiotherapy, University Hospital Utrecht, Heidelberglaan 100, 3584 CX Utrecht, The Netherlands

‡ Department of Radiology, University Hospital Utrecht, Heidelberglaan 100, 3584 CX Utrecht, The Netherlands

Received 6 February 1995, in final form 7 July 1995

Abstract. The aim of this study is to investigate and correct for machine- and object-related distortions in magnetic resonance images for use in radiotherapy treatment planning.

Patients with brain tumours underwent magnetic resonance imaging (MRI) in the radiotherapy position with the head fixed by a plastic cast in a Perspex localization frame. The imaging experiments were performed on a 1.5 T whole body MRI scanner with 3 mT m^{-1} maximum gradient capability. Image distortions, caused by static magnetic field inhomogeneity, were studied by varying the direction of the read-out gradient. For purposes of accuracy assessment, external and internal landmarks were indicated. Tubes attached to the cast and in the localization frame served as external landmarks. In the midsagittal plane the brain–sinus sphenoidalis interface, the pituitary gland–sinus sphenoidalis interface, the sphenoid bone and the corpora of the cervical vertebra served as internal landmarks. Landmark displacements as observed in the reversed read-out gradient experiments were analysed with respect to the contributions of machine-related static magnetic field inhomogeneity and susceptibility and chemical shift artifacts. The machine-related static magnetic field inhomogeneity in the midsagittal plane was determined from measurements on a grid phantom. Distortions due to chemical shift effects were estimated for bone marrow containing structures such as the sphenoid bone and the corpora of the cervical vertebra using the values obtained from the literature. Susceptibility-induced magnetic field perturbations are caused by the patient and the localization frame. Magnetic field perturbations were calculated for a typical patient dataset. The midsagittal head image was converted into a susceptibility distribution by segmenting the image into water-equivalent tissues and air; also the Perspex localization frame was included in the susceptibility distribution. Given the susceptibility distribution, the magnetic field was calculated by numerically solving the Maxwell equations for a magnetostatic field. Results were shown as magnetic field perturbations and corresponding spatial distortions of internal and external landmarks. The midsagittal head images were corrected for the machine imperfections (gradient non-linearity and static magnetic field inhomogeneity). The locations of the external landmarks in the frame were also corrected for susceptibility artifacts. The efficacy of the corrections was evaluated for these external landmarks in the localization frame with known geometry.

In this study at 1.5 T with read-out gradient strength of 3 mT m^{-1}, machine-related, chemical shift and susceptibility-induced static magnetic field inhomogeneity were of the same order, resulting in spatial distortions between −2 and 2 mm with only negative values for the chemical shift effect. Both the patient and the localization frame proved to perturb the magnetic field. The field perturbations were shown to be additive. In total, static magnetic field inhomogeneity led to spatial distortions ranging from −2 to 4 mm in the direction of the read-out gradient. Non-linearity of the gradients resulted in spatial distortions ranging from −3.5 to 0.5 mm. After correction for the machine imperfections and susceptibility artifacts, the geometric accuracy of the landmarks in the localization frame was better than 1.3 mm.

0031-9155/95/101651+14$19.50

1. Introduction

In radiotherapy treatment planning (RTP) accurate localization of tumour volume and critical organs and accurate placement of treatment fields is of major importance, because it enables the radiation dose to the tumour to be increased whilst allowing the dose to the surrounding dose limiting normal brain tissues to be minimized (Brahme 1984, Dutreix 1984, Goitein 1985, Mijnheer *et al* 1987, Suit and Du Bois 1991, Suit and Miralbell 1989). Of the different imaging modalities, magnetic resonance imaging (MRI) shows most promise for tumour localization for RTP because of its excellent soft-tissue contrast resolution and ability to scan in any plane orientation (Heesters *et al* 1993, Just *et al* 1991, Stark and Bradley 1992, TenHaken *et al* 1992). However, the introduction of MRI into RTP is seriously hampered by the geometric distortions of magnetic resonance (MR) images. MR image distortions are caused by non-linearity of the gradients and static magnetic field inhomogeneity. Field inhomogeneity is known to stem from the MRI scanner and from the magnetic properties of the object itself (Bakker *et al* 1992, Bhagwandien *et al* 1992, Ericsson *et al* 1988, Lüdeke *et al* 1985, Schad *et al* 1987b). The feasibility of measurement and correction of machine-related distortions has been demonstrated before (Bakker *et al* 1992, Schad *et al* 1987b, Sekihara *et al* 1984). The magnetic properties of the object induce the chemical shift and the susceptibility artifacts in MR images. The term 'chemical shift' is given to the variation in resonant frequency of a particular nucleus with molecular environment. The relative shift in the resonant frequency is caused by the local magnetic field due to the surrounding molecular structure. Protons in fat experience a magnetic field which is 3.2 parts per million (ppm) weaker than the magnetic field experienced by protons in water (Dixon 1984). In two-dimensional Fourier transform (2DFT) imaging, the read-out gradient relates the frequency of a proton to its location along the read-out gradient axis. The consequence for MRI is that the fat containing tissues will be shifted with respect to the other tissues. Susceptibility is the property which relates the magnetization of an object to the applied magnetic field. Susceptibility distributions lead to magnetic field perturbations, e.g. the presence of a patient in an MRI scanner will perturb the applied magnetic field because of the difference in susceptibility between the patient's body and the surrounding air. The severity of the field perturbations outside the body depends on the susceptibility difference with the surrounding air, the shape of the body and the orientation of the body with respect to the applied magnetic field. Field perturbations are more severe around protruding parts such as the extremities, the fingers of the hand and the nose. Inside the human body static magnetic field inhomogeneity is influenced by the shape of the body and the presence of local susceptibility inhomogeneities, e.g. the tissue–air interfaces around air cavities. External devices such as localization frames as used for RTP will also perturb the magnetic field. Correction methods for susceptibility-induced geometric distortions have been described and the efficacy has been demonstrated for the correction of distorted phantom images (Bakker *et al* 1992, Bhagwandien 1994, Chang and Fitzpatrick 1992, Cho *et al* 1988) and in a single case for the correction of an MR head scan (Sumanaweera *et al* 1993). Machine imperfections and magnetic properties of the object (chemical shift and susceptibility) lead to static magnetic field inhomogeneity. The resulting image distortions can be reduced by choosing maximum read-out and slice selection gradients (Bakker *et al* 1992, Chang and Fitzpatrick 1992). The aim of this work is to analyse and correct for image distortions in studies on patients with brain tumours, which were imaged in the radiotherapy position on a 1.5 T MRI scanner with the head fixed by a cast in a localization frame as described by (Leksell 1951). MRI compatible localization frames are widely used for image registration purposes. However, MRI compatibility does not mean that the applied magnetic field is

not perturbed and in our view this problem has not been fully explored yet. Magnetic field perturbations will be measured by means of reversed read-out gradient experiments. The contribution of susceptibility-induced magnetic field inhomogeneity will be analysed using a numerical method for calculating the magnetic field for arbitrary magnetic susceptibility distributions (Bhagwandien *et al* 1992). The efficacy of the methods for correction of distortions caused by non-linearity of the gradients and static magnetic field inhomogeneity will be investigated using the frame with known geometry.

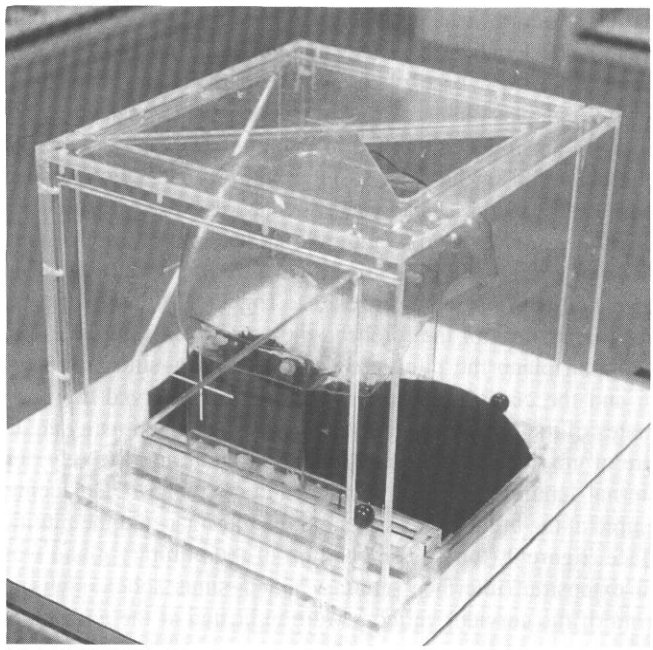

Figure 1. The localization frame with headcast and headrest.

2. Methods and materials

2.1. Experiments

Ten patients with brain tumours underwent MR scanning in the radiotherapy position on a flat table top with the head fixed by a plastic cast in a home-built localization frame. Imaging experiments were performed on a 1.5 T whole-body MRI scanner with 3 mT m^{-1} maximum gradient capability (Gyroscan S15, Philips Medical Systems, Best, The Netherlands). The pulse sequences were a conventional T_2-weighted spin echo sequence for tumour visualization (TR $\approx$ 2000 ms, TE = 30, 100 ms, NEX = 2, matrix = 256 $\times$ 256, number of slices $\approx$ 15, slice thickness = 5 mm, slice gap = 1 mm, FOV = 320 mm, offset = 60 mm anterior, magnitude reconstruction) and a T_1-weighted spin echo sequence with reversed read-out gradient for the study of image distortions caused by static magnetic field inhomogeneity (TR $\approx$ 900 ms, TE = 30 ms, other parameters as above). These datasets, acquired with opposite directions of the read-out gradient, enable the study of image distortions caused by static magnetic field inhomogeneity. Since static magnetic field inhomogeneity results in spatial distortions in the direction of the read-out gradient, the true position (apart from distortions caused by gradient errors) of an image structure is half-way

between the two distorted positions in both datasets (Chang and Fitzpatrick 1992). In the following, a spatial distortion is defined as the distance between the true position and the distorted position and a displacement is defined as the distance between two positions in images acquired with opposite directions of the read-out gradient. Distortions caused by static magnetic field inhomogeneity are inversely proportional to the strength of the read-out gradient; this gradient was chosen to be a maximum (3 mT m^{-1}) to give minimal distortions. In the experiments at 1.5 T with read-out gradient strength of 3 mT m^{-1}, static magnetic field inhomogeneity results in spatial distortions of 0.5 mm per ppm. Although beyond the scope of this study, the slice selection gradient was also chosen to be a maximum (3 mT m^{-1}) to reduce plane warp. The localization frame is shown in figure 1. The plastic cast and the frame are both attached to a base plate, so that patient and frame can be positioned reproducibly. The five Perspex plates of the frame and the base form a box, open at the caudal end, with outer dimensions width×height×length = 30 cm×27 cm×27 cm. This set-up fits closely in the body coil of the MRI scanner and provides enough space for a patient to be positioned with the head on a headrest, which is also used during radiotherapy. For purposes of accuracy assessment, external and internal landmarks were chosen. Plastic tubes with an inner diameter of 2 mm, filled with doped water (770 mg $CuSO_4.5H_2O$ l^{-1}), were set in a Z shape in grooves milled in the Perspex plates. Together with three tubes attached to the cast of the patient at the position of the forehead they served as external landmarks (figure 2 (top)). In the midsagittal plane the pituitary gland, the brain–sinus sphenoidalis interface, the sphenoid bone and the corpora of the cervical vertebra served as internal landmarks. The image coordinates of the external landmarks were determined using an algorithm which calculates the centre of gravity of signal intensities within an interactively positioned square of pixels. The internal landmarks were indicated interactively. Displacements around air cavities were measured at the brain–sinus sphenoidalis interface and the pituitary gland–sinus sphenoidalis interface (figure 2 (top)). The position of the pituitary gland was characterized by its most caudal extension (interface pituitary gland–sinus sphenoidalis). The sphenoid bone and the corpora of the cervical vertebra were indicated at the corner points. For these structures the displacements of the corner points were averaged to obtain the displacement of each structure.

2.2. *Analysis*

The landmark displacements, as observed in the reversed read-out gradient experiments, originate from machine-related static magnetic field inhomogeneity, susceptibility and chemical shift artifacts. The experiments reveal total displacements; the different contributions cannot be separated. The contribution of machine-related static magnetic field inhomogeneity could be determined from measurements on a grid phantom (see subsection 2.3). Contributions of chemical shift effects are to be expected for bone marrow containing structures such as the sphenoid bone and the corpora of the cervical vertebra. Values for these contributions were obtained from the literature. The contribution of susceptibility-induced magnetic static magnetic field inhomogeneity was numerically calculated.

Susceptibility-induced field perturbations may be caused by the patient and the localization frame. The susceptibility-induced magnetic field perturbations were calculated for a typical patient in this study. The midsagittal MR image was converted into a susceptibility distribution by segmenting the image into water-equivalent tissue (soft tissues and bone, susceptibility $\chi = -9 \times 10^{-6}$) and air ($\chi = 0$). This is a fair approximation, since significant susceptibility inhomogeneities only occur at tissue–air interfaces. Soft tissues,

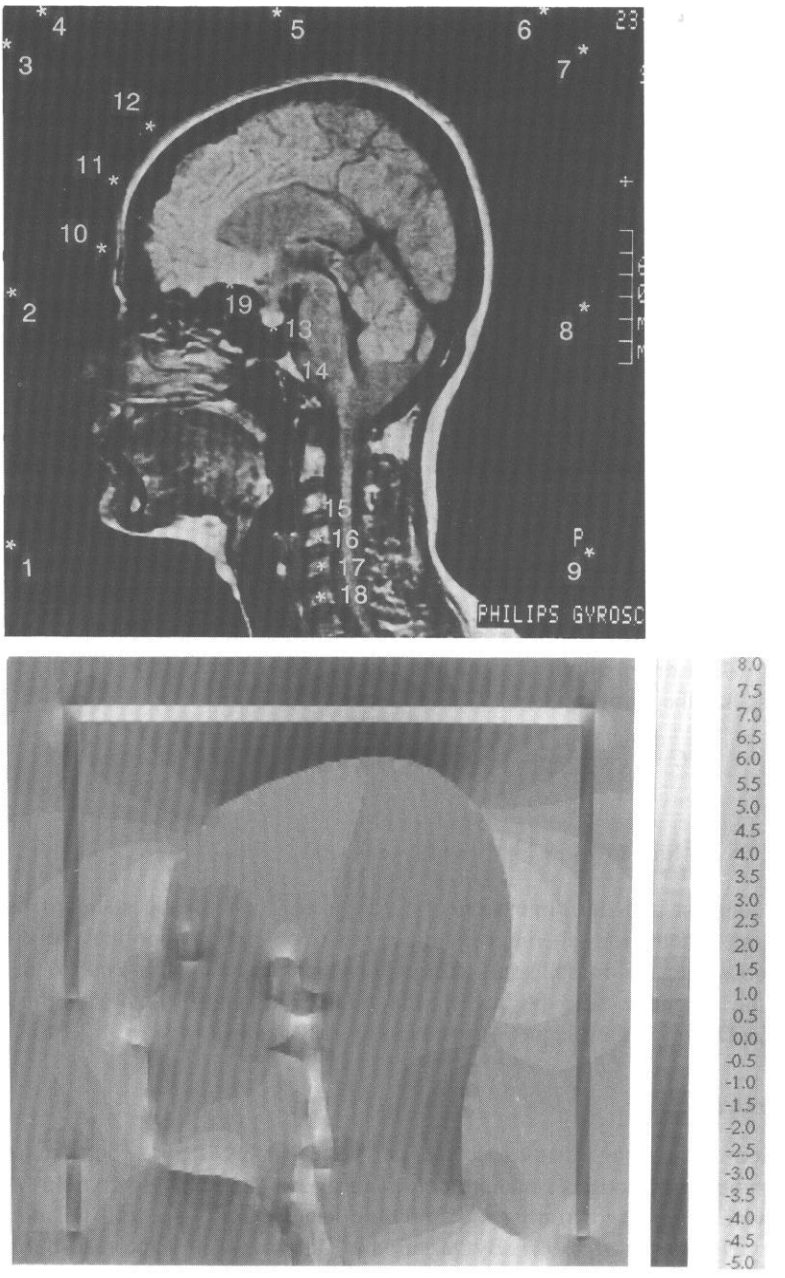

Figure 2. Top, midsagittal MR head image with internal and external landmarks indicated: 1–9, external landmarks in the localization frame; 10–12, external landmarks attached to the cast at the forehead; 13, pituitary gland; 14, sphenoid bone; 15–18, corpora of the cervical vertebra; 19, interface brain–sinus sphenoidalis. Bottom, calculated magnetic field perturbations in the midsagittal plane. The perturbations are shown by means of shades with a step size of 0.5 ppm. Light shades indicate a stronger field, dark shades indicate a weaker field than the 1.5 T magnetic field, applied in the caudocranial direction. The head was segmented into soft tissues, bone and Perspex, $\chi = -9 \times 10^{-6}$, and air, $\chi = 0$. Note the variation in magnetic field perturbation with the orientation of the Perspex plates.

blood and bone show susceptibilities ranging from -7.5 to -10×10^{-6} (Bhagwandien 1994, Sumanaweera *et al* 1993, Weast and Astle 1980, Weisskoff and Kiihne 1992). The Perspex frame was included in the susceptibility distribution guided by the location of the tubes, which were clearly visible in the MR images (figure 2 (top)). The susceptibility of Perspex was determined from reversed read-out gradient experiments on a coaxial cylinder with a Perspex inner region and the annular region filled with water (Lüdeke *et al* 1985, Sumanaweera *et al* 1993). Spin echo and gradient echo images were acquired with minimal read-out gradient ($G = 0.85$ mT m^{-1}) to obtain maximal sensitivity for visualization of susceptibility-induced image distortions. Nevertheless, the images showed no susceptibility artifacts, from which we could conclude that the susceptibility of Perspex is equal to that of water: $\chi_{\text{Perspex}} = -9 \times 10^{-6}$. Given this susceptibility distribution, the magnetic field was calculated by numerically solving the Maxwell equations (Bhagwandien *et al* 1992, 1994). In the following we will give a brief description of the method. The Maxwell equations for magnetostatic problems reduce to the Laplace equation

$$\nabla \cdot (\mu \nabla \Phi_M) = 0 \tag{1}$$

where μ is the magnetic permeability (dimensionless) ($\mu = 1 + \chi$), χ the magnetic susceptibility (dimensionless) and Φ_M the magnetic scalar potential (Wb m^{-1}). For a given μ-distribution, Φ_M is determined by (numerically) solving (1). This is done by transforming (1) into a diffusion equation with the introduction of an iteration coordinate τ (a pseudotime). The stationary state of the diffusion equation is then the magnetic scalar potential (Φ_M) distribution. This means that the general definition of convergence of such a process has the form

$$C \frac{d\Phi_M(x, y, z; \tau)}{d\tau} = \nabla \cdot (\mu(x, y, z) \nabla \Phi_M(x, y, z; \tau)) \tag{2}$$

where

$$\lim_{\tau \to \infty} \Phi_M(x, y, z; \tau) = \Phi_M(x, y, z). \tag{3}$$

C is a constant and the dimension of $C/d\tau$ is m^{-2}. With the standard finite-difference Fourier implementation scheme, which involves two iteration coordinate levels at coordinate τ and coordinate $\tau + d\tau$, the solution is achieved for a rectangular grid. With $\boldsymbol{H} = -\nabla \Phi_M$ ($\boldsymbol{H}$ is the magnetic field (A m^{-1})), the induced magnetic field $\boldsymbol{B}$[T] is calculated as $\boldsymbol{B} = \mu_0 \mu \boldsymbol{H}$ (μ_0 is the magnetic permeability in vacuum ($4\pi \times 10^{-7}$ H m^{-1})).

2.3. Correction

Correction of the image distortions was performed in two steps. The first step corrects for the machine imperfections (gradient non-linearity and static magnetic field inhomogeneity), which were determined from sets of multiple slice images of a grid phantom with known geometry (Bakker *et al* 1992). By variation of the direction of the read-out gradient, static field and gradient field errors were determined at the phantom tube positions, from which 3D error maps were inferred by bicubic interpolation. Patient images were corrected using the error maps and taking into account actual gradient directions, strengths, field of view and offsets. The second step corrects for the object-related image distortions, *viz.* the chemical shift and susceptibility-induced image distortions. The necessary corrections were determined from the displacements in images, which were acquired with opposite directions of the read-out gradient and which were corrected for machine-related static magnetic field inhomogeneity and non-linearity of the gradients. The true position of an image structure is half-way between the two distorted positions in both images. The efficacy of the methods to

correct for machine-related and object-related image distortions was evaluated for landmarks at defined locations, *viz.* the external landmarks 1, 3, 4, 6, 7 and 9 in the localization frame. The frame coordinate system was related to the coordinate system of the MR image, which was corrected for machine- and object-related image distortions. The frame coordinates and the corrected image coordinates of the external landmarks 1, 3, 4, 6, 7 and 9 were matched using an algorithm for least-squares fitting of two 3D point sets (Arun *et al* 1987). The real frame coordinates were thus transformed into image coordinates, which were taken as the true image coordinates. Spatial distortions of external landmarks in uncorrected and corrected images were evaluated with respect to these true image coordinates.

3. Results and discussion

3.1. Experiments

Reversed gradient images were acquired from 10 patients, of which three patients were imaged with the localization frame attached to the base of the patient's headcast. Internal landmark displacements were measured in all patient studies, the displacements of the external landmarks in the frame (1–9) in three patient studies and the external landmarks attached to the cast at the location of the forehead (10, 11, 12) in seven patient studies. For this patient set-up and the applied scan protocol the mean spatial image distortions caused by static magnetic field inhomogeneity were systematic, ranging from −2 to 4 mm with a standard deviation of 0.5 mm for the external landmarks and 1 mm for the internal landmarks (figure 3(*a*)).

3.2. Analysis

The image distortions were analysed with respect to the contributions of the different sources of static magnetic field inhomogeneity for a typical patient imaged in the localization frame.

3.2.1. Machine-related static magnetic field inhomogeneity. The machine-related static magnetic field inhomogeneity in the midsagittal plane was determined from the measurements on a grid phantom. The asterisks in figure 3(*b*) denote the machine-related field errors in parts per million (right-hand ordinate) and corresponding spatial distortions in millimetres (left-hand ordinate) at the locations of the internal and external landmarks. In the experiments at 1.5 T with read-out gradient strength of 3 mT m^{-1}, static magnetic field inhomogeneity results in spatial distortions of 0.5 mm per ppm. Machine-related static magnetic field inhomogeneity resulted in mean spatial distortions ranging from −0.5 to 1.5 mm.

3.2.2. The chemical shift effect. In this study, bone marrow containing internal structures were the sphenoid bone and the corpora of the cervical vertebra. The sphenoid bone and the corpora of the cervical vertebra showed different signal intensities and spatial distortions (figures 2 (top) and 3(*b*)). The contribution of chemical shift effects was estimated from values in the literature as follows. In the normal human adult, bone marrow can be divided into yellow (fatty marrow) and red (haematopoietic marrow) (Bloom and Fawcett 1968). The sphenoid bone marrow signal is bright, comparable to subcutaneous fat (figure 2 (top)). This suggests yellow bone marrow in the sphenoid bone (Wismer *et al* 1985), which results in a chemical shift of −3.2 ppm (triangle for landmark 14 in figure 3(*b*)). Vertebrae contain red marrow, about 70% of which is composed of cellular elements containing mostly water

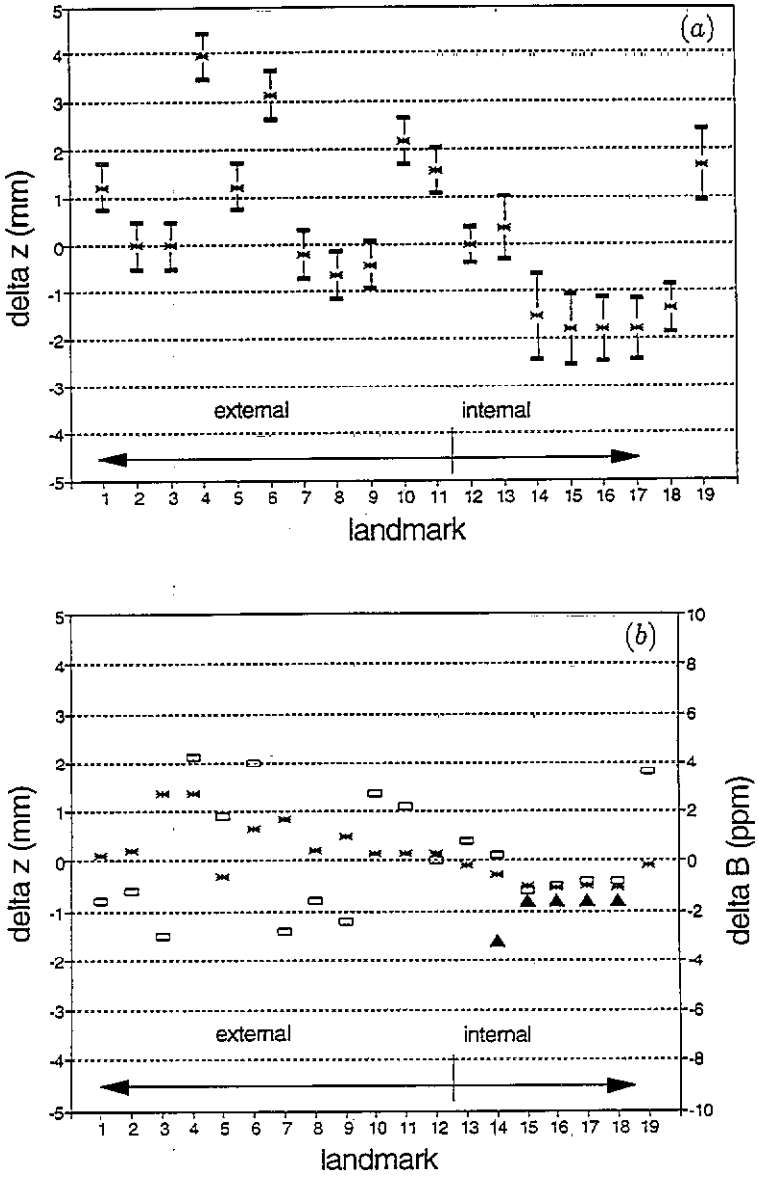

Figure 3. (*a*) spatial image distortions (delta *z*) in the midsagittal plane caused by static magnetic field inhomogeneity according to the reversed read-out gradient experiments on 10 patients (average ± standard deviation). The read-out gradient strength was 3 mT m^{-1}. (*b*) field inhomogeneity (delta *B*) and resulting spatial image distortions (delta *z*) in the midsagittal plane caused by machine-related static field inhomogeneity (asterisks), chemical shift (triangles) and susceptibility-induced (rectangles) static magnetic field inhomogeneity. Field inhomogeneity is expressed in parts per million (right-hand ordinate), corresponding spatial distortions in millimetres (left-hand ordinate). The read-out gradient strength was 3 mT m^{-1}. Analysis for a typical patient. (*c*) comparison between measured static magnetic field inhomogeneity or corresponding spatial distortions (rectangles) and sum of contributions (asterisks) from machine-related static magnetic field inhomogeneity (measurement), chemical shift (literature values) and susceptibility-induced static magnetic field inhomogeneity (numerical calculation). Analysis for a typical patient.

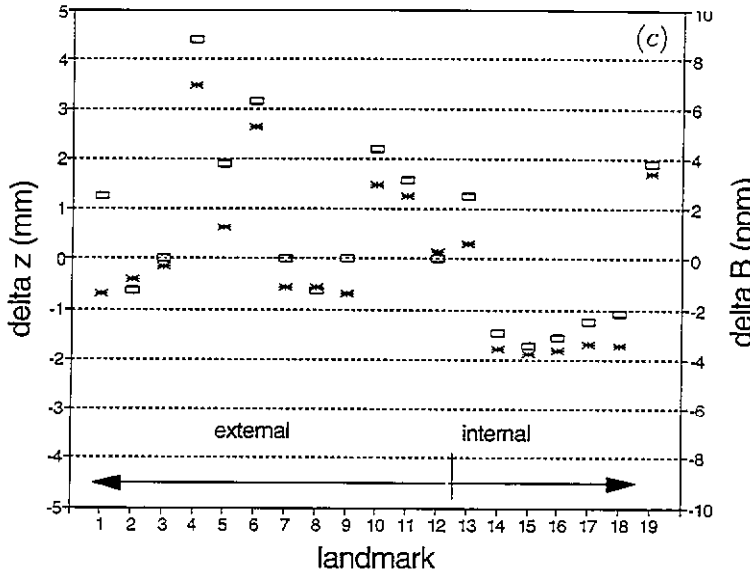

Figure 3. (Continued)

protons; the remainder consists of fat, intimately admixed with the cellular elements (Cristy 1981). The admixture of fat and water constituents is such that high fractional volumes of each contribute signal to the image voxel (Wismer *et al* 1985), which resulted in about one-half of the chemical shift because of partial volume effects (triangles for landmarks 15–18 in figure 3(*b*)).

3.2.3. Susceptibility-induced static magnetic field inhomogeneity. The patient and the localization frame perturbed the applied magnetic field of 1.5 T, which is along the caudocranial direction (figure 2 (bottom)). Calculation of the magnetic field revealed that, on average, the field strength in the patient's brain was 0.8 ppm above the applied field of 1.5 T. Spatial landmark distortions were measured with respect to the position of the brain tissue, which showed no displacements in the reversed read-out gradient experiments. Therefore, magnetic field strengths at different locations will be expressed as deviations (in parts per million) from the magnetic field strength in the brain tissue. The field strength in the frame proved to be dependent on the orientation of the plates with respect to the main magnetic field. The field perturbation in the posterior and anterior plates, which were parallel to the magnetic field, was about −2 ppm (rectangles for landmarks 1–3 and 7–9 in figure 3(*b*)). The field perturbation in the cranial plate, which was perpendicular to the magnetic field, was maximally 4.2 ppm (rectangles for landmarks 4–6 in figure 3(*b*)). The field perturbation at the position of landmark 5 in the middle of the cranial plate was partly cancelled by the magnetic field perturbation by the patient's head resulting in a total field deviation of 2 ppm.

The magnetic field around the head resulted in displacements of the tubes attached to the cast of the patient. Depending on the position, susceptibility-induced field perturbations ranged from 0–3 ppm (rectangles for landmarks 10–12 in figure 3(*b*)).

Also inside the head local susceptibility inhomogeneities lead to magnetic field perturbations, e.g. at the interface between tissue and air cavities such as the sinus sphenoidalis. The susceptibility-induced field perturbations at the interfaces of the sinus

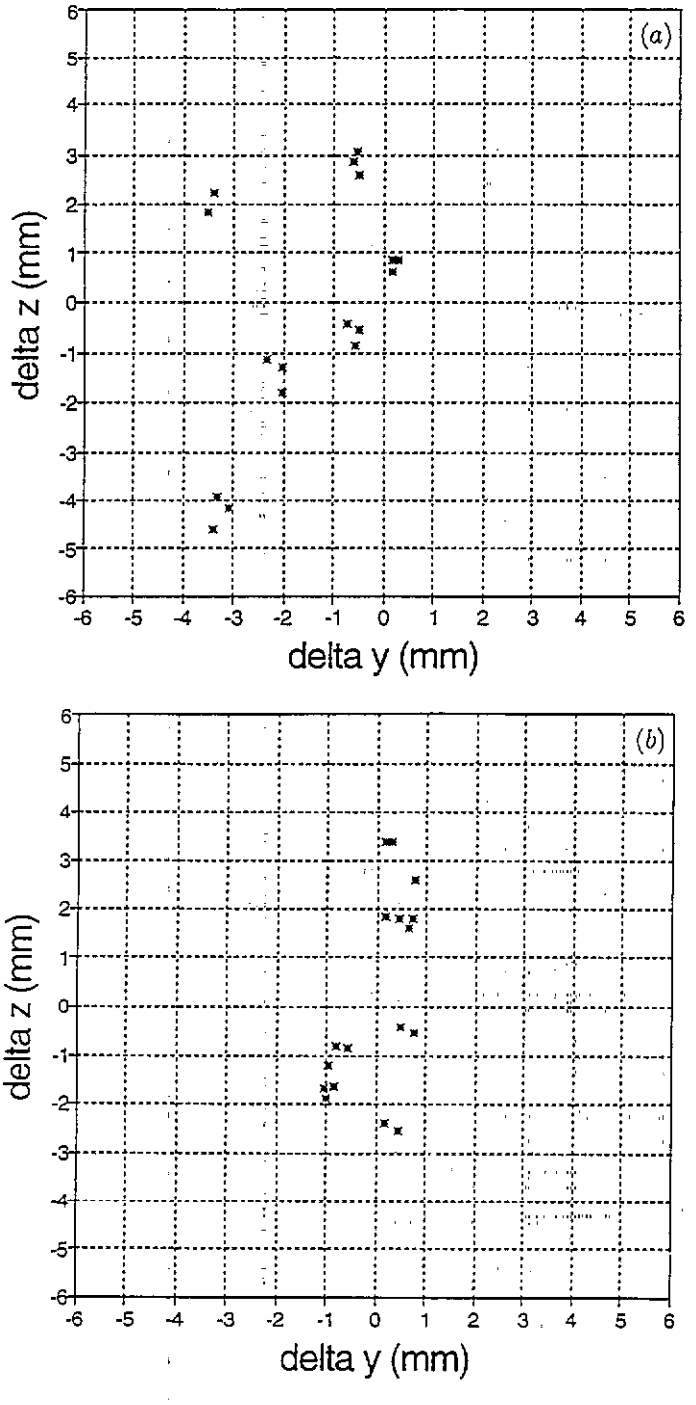

Figure 4. Spatial distortions (delta *y*, delta *z*) of the external landmarks 1, 3, 4, 6, 7 and 9 in the localization frame in MR images of three patient studies. The phase encoding gradient was directed along the *y* axis; the read-out gradient was directed along the *z* axis. (*a*) spatial distortions in uncorrected MR images. (*b*) spatial distortions in MR images corrected for machine imperfections. (*c*) spatial distortions in MR images corrected for machine imperfections and susceptibility artifacts.

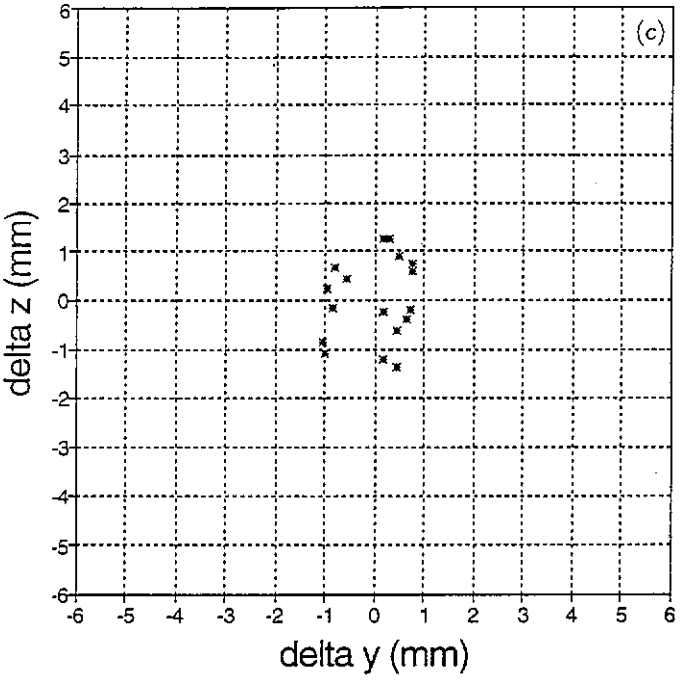

Figure 4. (Continued)

sphenoidalis with the pituitary gland and the brain tissue were respectively 0.8 and 3.6 ppm (rectangles for landmarks 13 and 19 in figure 3(*b*)). The smaller size of the neck area with respect to the head resulted in a susceptibility-induced field perturbation of about −1 ppm at the position of the cervical spine (rectangles for landmarks 15–18 in figure 3(*b*)).

3.2.4. Total static magnetic field inhomogeneity. The analysis of MR image distortions is rather complicated because of the contributions of different sources of magnetic field inhomogeneity apart from distortions by gradient non-linearity. In this study mean spatial image distortions caused by static magnetic field inhomogeneity ranged from −2 to 4 mm. Matching of a midsagittal MR image with a lateral simulator film based on bony structures like the corpora of the cervical vertebra could result in a mismatch as large as 6 mm for landmark 4 in the frame (figure 3(*a*)). For an accurate use of MR images for RTP, it is important to know the image distortions and from what error source they are originating. In this study at 1.5 T with read-out gradient strength of 3 mT m^{-1} the respective contributions of machine-related, chemical shift and susceptibility-induced spatial distortions of landmarks were of the same order, ranging from −2 to 2 mm with only negative values for the chemical shift effect. The observed mean total distortions ranging from −2 to 4 mm could be ascribed to the contributions from machine-related, chemical shift and susceptibility-induced static magnetic field inhomogeneity. An exception is landmark 1, of which the observed distortion deviated about 2 mm from the expected value (figure 3(*c*)). This may be explained by errors in calculating the susceptibility-induced magnetic field perturbations, since the magnetic field was calculated for the head and neck region instead of the total body.

Our analysis of object-related image distortions was based on studies on a 1.5 T MRI scanner with 3 mT m^{-1} gradient capability, but the results are more widely of interest.

Although nowadays MRI scanners are mostly equipped with 10 mT m^{-1} gradients, in clinical practice the read-out gradient is usually operated up to about 3 mT m^{-1} in order to have sufficient signal to noise ratio. Furthermore, the object-related image distortions as measured in this study can be directly extrapolated to distortions to be expected at different static and gradient field strengths, since they are proportional to the main magnetic field strength and inversely proportional to the read-out gradient strength. In 0.5 T magnetic resonance images acquired with the same read-out gradient strength as applied in this study (3 mT m^{-1}), image distortions will be a factor of three smaller. At 0.5 T for this patient set-up, distortions caused by static magnetic field inhomogeneity can be reduced to 1.5 mm, which is of the order of the pixel size. However, each system, irrespective of the static field strength or the gradient field strength, should be checked for image distortions caused by gradient non-linearity. In our experience with different MRI scanners, increase of gradient capability does not imply improvement of gradient linearity.

3.3. Correction method

The efficacy of the correction method was evaluated for the external landmarks 1, 3, 4, 6, 7 and 9 in the localization frame, since for these landmarks the real geometry is known. Figure 4(*a*) shows the spatial distortions in the uncorrected midsagittal MR images of the three patients which were imaged in the frame. Mean spatial distortions in the y direction between −3.5 and 0.5 mm were caused by non-linearity of the y gradient, which was the phase encoding gradient. Spatial distortions in the z direction were larger, ranging from −4.5 to 3 mm. These distortions were caused by non-linearity of the read-out gradient and machine-related and susceptibility-induced static magnetic field inhomogeneity. Figure 4(*b*) shows the results after correction for the machine imperfections. Accuracy in the y direction was better than 1.3 mm and in the z direction distortions ranged from −2.5 mm to 3.5 mm, which indicated that susceptibility artifacts had also to be corrected for. Figure 4(*c*) shows the results after correction for all sources of distortion. Residual errors are of the order of 1.3 mm, which may be explained by the MR image resolution (the pixel size is 1.25 mm × 1.25 mm) and inaccuracies in the numerical calculation of the susceptibility-induced magnetic field perturbations. In principle, the correction scheme will lead to the same accuracy for the patient structures. This is more difficult to evaluate, since the real geometry is unknown in these studies. In the future, uncorrected and corrected MR datasets will be compared with computerized tomography (CT) datasets for accuracy assessment.

Geometric accuracy is a need if MR images are to be used as the only input for RTP. A different approach is the use of both CT and MRI. These methods rely on CT for geometric accuracy and on MRI for tumour visualization (Van den Elsen 1993, Fraass *et al* 1987, Kessler *et al* 1991, Kooy *et al* 1994, Pelizzari *et al* 1989, Schad *et al* 1987a). This approach requires matching of the two datasets, which theoretically can better be accomplished if MR image distortions have been reduced by pulse sequence optimization or if the distortions have been corrected.

4. Conclusions

In this study at 1.5 T with read-out gradient strength of 3 mT m^{-1} the respective contributions of machine-related, chemical shift and susceptibility-induced spatial distortions were of the same order, ranging from −2 to 2 mm with only negative values for the chemical shift effect. The observed mean total distortions ranging from −2 to 4 mm could be ascribed to the

contributions from machine-related, chemical shift and susceptibility-induced static magnetic field inhomogeneity. Non-linearity of the gradients resulted in spatial distortions ranging from −3.5 to 0.5 mm. After correction for the machine imperfections and susceptibility artifacts, the geometric accuracy of the landmarks in the localization frame was of the order of the pixel size.

Acknowledgment

This work is supported by the Dutch Cancer Society (grant IKMN 90-04).

References

Arun K S, Huang T S and Blostein S D 1987 Least-squares fitting of two 3-D point sets *IEEE Trans. Pattern Anal. Machine Intell.* **PAMI-7** 698–700

Bakker C J G Moerland M A Bhagwandien R and Beersma R 1992 Analysis of machine-dependent and object-induced geometric distortions in 2DFT MR imaging *Magn. Reson. Imaging* **10** 597–608

Bhagwandien R 1994 Object induced geometry and intensity distortions in magnetic resonance imaging *PhD Thesis* University of Utrecht

Bhagwandien R, Moerland M A, Bakker C J G, Beersma R and Lagendijk J J W 1994 Numerical analysis of the magnetic field for arbitrary magnetic susceptibility distributions in 3D 1994 *Magn. Reson. Imaging* **12** 101–7

Bhagwandien R, van Ee R, Beersma R, Bakker C J G, Moerland M A and Lagendijk J J W 1992 Numerical analysis of the magnetic field for arbitrary magnetic susceptibility distributions in 2D *Magn. Reson. Imaging* **10** 299–313

Bloom W and Fawcett D W A 1968 *Textbook of Histology* (Philadelphia: Saunders)

Brahme A 1984 Dosimetric precision requirements in radiation therapy *Acta Radiol. Oncol.* **23** 379–91

Chang H and Fitzpatrick J M A 1992 Technique for accurate magnetic resonance imaging in the presence of field inhomogeneities *IEEE Trans. Med. Imaging* **MI-11** 319-29

Cho Z H, Kim D J and Kim Y K 1988 Total inhomogeneity correction including chemical shifts and susceptibility by view angle tilting *Med. Phys.* **15** 7–11

Cristy M 1981 Active bone marrow distribution as a function of age in humans *Phys. Med. Biol.* **26** 389–400

Dixon W T 1984 Simple proton spectroscopic imaging *Radiology* **153** 189–94

Dutreix A 1984 When and how can we improve precision in radiotherapy *Radiother. Oncol.* **2** 275–92

Ericsson A, Hemmingsson A, Jung B and Sperber G O 1988 Calculation of MRI artifacts caused by static field disturbances *Phys. Med. Biol.* **33** 1103–12

Fraass B A, McShan D L, Diaz R F, TenHaken R K, Aisen A, Gebarski S, Glazer G and Lichter A S 1987 Integration of magnetic resonance imaging into radiation therapy treatment planning: I. Technical considerations *Int. J. Radiat. Oncol. Biol. Phys.* **13** 1897–908

Goitein M 1985 Calculation of the uncertainty in the dose delivered during radiation therapy *Med. Phys.* **12** 608–12

Heesters M A A M, Wijrdeman, H K, Struikmans H, Witkamp T D and Moerland M A 1993 Brain tumour delineation based on CT and MR imaging; implications for radiotherapy treatment planning *Strahlenther. Onkol.* **12** 729–33

Just M, Rösler H P, Kutzner J and Thelen M 1991 MRI-assisted radiation therapy planning of brain tumors—clinical experiences in 17 patients *Magn. Reson. Imaging* **9** 173–7

Kessler M L, Pitluck S, Petti P and Castro J R 1991 Integration of multimodality imaging data for radiotherapy treatment planning *Int. J. Radiat. Oncol. Biol. Phys.* **21** 1653–67

Kooy H M, Van Herk M B, Barnes P D, Alexander E III, Dunbar S F, Tarbell N J, Mulkern R V, Holupka E J and Loeffler J S 1994 Image fusion for stereotactic radiotherapy and radiosurgery treatment planning *Int. J. Radiat. Oncol. Biol. Phys.* **28** 1229–34

Leksell L 1951 The stereotaxic method and radiosurgery of the brain *Acta Chir. Scand.* **102** 316–19

Lüdeke K M, Röschmann P and Tischler R 1985 Susceptibility artifacts in NMR imaging *Magn. Reson. Imaging* **3** 329–43

Mijnheer B J, Battermann J J and Wambersie A 1987 What degree of accuracy is required and can be achieved in photon and neutron therapy? *Radiother. Oncol.* **8** 237–52

Pelizzari C A, Chen G T Y, Spelbring D R, Weichselbaum R R and Chen C T 1989 Accurate three-dimensional registration of CT, PET, and/or MR images of the brain *J. Comput. Assist. Tomogr.* **13** 20–6

Schad L R, Boesecke R, Schlegel W, Hartmann G H, Sturm V, Strauss L G and Lorenz W J 1987b Three dimensional image correlation of CT, MR, and PET studies in radiotherapy treatment planning of brain tumors *J. Comput. Assist. Tomogr.* **11** 948–54

Schad L R, Lott S, Schmitt F, Sturm V and Lorenz W J 1987a Correction of spatial distortion in MR imaging: a prerequisite for accurate stereotaxy *J. Comput. Assist. Tomogr.* **11** 499–505

Sekihara K, Kuroda M and Kohno H 1984 Image restoration from non-uniform magnetic field influence for direct Fourier NMR imaging *Phys. Med. Biol.* **29** 15–24

Stark D D and Bradley W G 1992 *Magnetic Resonance Imaging* (Chicago: Mosby Year Book)

Suit H D and Du Bois W 1991 The importance of optimal treatment planning in radiation therapy *Int. J. Radiat. Oncol. Biol. Phys.* **21** 1471–8

Suit H D and Miralbell R 1989 Potential impact of improvements in radiation therapy on quality of life and survival *Int. J. Radiat. Oncol. Biol. Phys.* **16** 891–5

Sumanaweera T S, Glover G H, Binford T O and Adler J R 1993 MR susceptibility misregistration correction *IEEE Trans. Med. Imaging* **MI-12** 251–9

TenHaken R K, Thornton A F, Sandler H M, LaVigne M L, Quint D J, Fraass B A, Kessler M L and McShan D L A 1992 Quantitative assessment of the addition of MRI to CT-based, 3-D treatment planning of brain tumors *Radiother. Oncol.* **25** 121–33

Van den Elsen P A 1993 Multimodality matching of brain images *PhD Thesis* University of Utrecht

Weast R C and Astle M J 1980 *CRC Handbook of Chemistry and Physics* (Boca Raton, FL: Chemical Rubber Company)

Weisskoff R M and Kiihne S 1992 MRI susceptometry: image-based measurement of absolute susceptibility of MR contrast agents and human blood *Magn. Reson. Med.* **24** 375–83

Wismer G L, Rosen B R, Buxton R, Stark D D and Brady T J 1985 Chemical shift imaging of bone marrow *Am. J. Roentgenol.* **145** 1031–7